

# Numerical simulation on excavation-induced damage of rock under quasi-static unloading and dynamic disturbance

Leilei Niu<sup>1</sup> · Wancheng Zhu<sup>1</sup> · Zhen Cheng<sup>1</sup> · Kai Guan<sup>1</sup> · Tao Qin<sup>1</sup>

Received: 10 December 2016 / Accepted: 29 August 2017 / Published online: 4 September 2017  
© Springer-Verlag GmbH Germany 2017

**Abstract** During the excavation of underground opening, the rock may experience a complex loading path that includes the highly confined compression before excavation, unloading of confining stress and further disturbance of dynamic loading after excavation. By using Rock Failure Process Analysis for Dynamics (RFPA-Dynamics), the failure of rock sequentially subjected to this complex loading path is numerically simulated, in order to examine the rock failure mechanism induced by excavation. The RFPA-Dynamics is firstly used to reproduce the failure of rock under confined compression, followed by unloading of confining pressure, and it is validated against with the existing experimental observation. Then, the failure characteristics of rock specimen sequentially subjected to the quasi-static triaxial loading, unloading of confining pressure and dynamic disturbance are numerically simulated, where the effect of magnitude of axial loading and confining pressure, and duration and amplitude of the dynamic disturbance on the final failure patterns of rock are examined. The numerical results indicate that the arc-shaped spalling damage zone is prone to develop with the increase in the axial pressure and lateral pressure coefficient. As for the effect of dynamic disturbance, the contribution of duration and amplitude of dynamic disturbance on the energy input are similar, where the area of damage zone increases with the energy input into the rock specimen. In this regard, the area of the damage zone is influenced by both the magnitude of in situ stress and waveform of

dynamic disturbance. This study denotes that it is of great significance to trace the complex loading path induced by excavation in order to capture the rock failure mechanism induced by underground excavation.

**Keywords** Excavation-induced damage · Unloading of confining stress · Dynamic disturbance · Numerical simulation

## Introduction

In the past few decades, when the mining operation goes deeper, the mechanical response of rock around deep excavation has been observed different from that at the shallow depth. In particular, the dynamic effect induced by excavation would be a very important factor affecting the development excavation damaged zone (EDZ) (Zhu et al. 2014a). During the underground excavations such as mining opening, tunnel, nuclear waste repository and underground protective engineering, the surrounding rock masses may undergo a complex loading and unloading process, especially under high in situ stress. Deep rock is subjected to high in situ stress (quasi-static triaxial stress) before excavation and the unloading owing to the formation of free surface which gives rise to stress change from original three-dimensional to two-dimensional or one-dimensional state. In addition, the excavation surface may experience dynamic disturbance such as rock blasting, which may trigger the occurrence of unstable failure of surrounding rock mass. Therefore, the failure characteristic of rock sequentially subjected to the quasi-static triaxial loading, unloading of confining pressure and dynamic disturbance defines one of the most important mechanisms

✉ Wancheng Zhu  
zhuwancheng@mail.neu.edu.cn

<sup>1</sup> Center for Rock Instability and Seismicity Research, School of Resource and Civil Engineering, Northeastern University, Shenyang 110819, China

that excavation might induce the unstable rock failure such as rock bursts (Wu and Liu 2009; Zhao and Wang 2010).

Currently, more attention is paid to study the influence of stress unloading on the failure of rock as a result of excavation activities. Extensive studies have been performed to investigate the unloading mechanism and predict the extent of excavation damaged zone (Falls and Young 1998; Backblom and Martin 1999; Diederichsa et al. 2004; Read 2004; Martino and Chandler 2004). In this respect, many theoretical models, laboratory and in situ experiments and numerical simulations are conducted. Cai and Kaiser (2005) presented a method to quantify the degree of damage and to characterize the excavation damaged zone (or excavation disturbed zone) based on microseismic monitoring data. Guan et al. (2007) reported two categories of theoretical methods for ground reaction analyses in conventional tunneling excavation, in which one of them the unloading process of ground is taken into account. The non-Euclidean dynamic model is proposed to investigate the zonal disintegration mechanism of isotropic rock masses around a deep circular tunnel subjected to dynamic unloading (Zhou and Shou 2013). Yang et al. (2014) simplified the analysis on the possible excavation damaged zone around a tunnel where the constitutive curve under loading and unloading is adopted. An exact closed-form analytical solution for the ground response around cylindrical and spherical openings unloaded from isotropic and uniform stress states was proposed by Vrakas and Anagnostou (2014). Moreover, a series of representative unloading experiments (Hua and You 2001; Corkum and Martin 2007b; Malmgren et al. 2007; Zhou et al. 2008) on rocks were carried out to clarify the fracture features observed from the underground workshop excavation zone. Based on many physical and numerical model tests, Sellers and Klerck (2000) investigated the behavior of the rock surrounding circular excavations during loading and unloading. Bossart et al. (2002) analyzed the geological and hydraulic characterization of the excavation disturbed zone. Fakhimi et al. (2002) performed a biaxial compression test on a sandstone specimen with a circular opening to simulate the failure around an underground excavation in brittle rock. The mechanism of crack initiation, propagation and interaction was also studied in deep tunneling in brittle rock with continuous excavation (Diederichsa et al. 2004). Conventional triaxial unloading tests were also conducted to reveal the characteristics of stress–strain relation, deformation, damage, modulus and strength under unloading conditions (Huang et al. 2001; Xie and He 2004). The rock-burst process under true triaxial unloading was monitored by using the acoustic emission monitoring technique (He et al. 2010; He and Zhao 2013). The experiment of the thick-walled hollow cylindrical specimens subjected to a mechanical unloading to mimic a

gallery excavation was carried out to investigate the excavation damaged zone (EDZ) around Opalinus Clay and the nuclear waste disposal in clay formations (Labiouse and Vietor 2014). Axisymmetric triaxial loading–unloading tests are conducted on marble specimens with initial different confining pressures and unloading rates (Huang and Li 2014). Using a true triaxial state test condition, one side of the specimen was unloaded to model the excavation and study the phenomenon of splitting failure in the rock mass adjacent to an underground excavation in a region of high initial stresses (Zhu et al. 2014b).

In addition to these theoretical models and experimental studies, numerical simulation is also conducted to analyze the failure mechanism and pattern under excavation-induced unloading. Three extensions to the discontinuous deformation analysis (DDA) method, as suggested by Kim et al. (1999), consisted of hydromechanical coupling between rock blocks and steady water flow in fractures, sequential loading or unloading, and rock reinforcement, were used to simulate underground excavation in fractured rock. A study of bifurcation in the problem of unloading a circular excavation in a strain-softening rock mass is investigated with the FDM-based code (Varas et al. 2005). The unloading processes of rocks under high initial triaxial stress were analyzed by the finite element method with continuous surface cap model (CSCM) (Tao et al. 2012, 2013) and damage-based model (Zhu et al. 2014a), respectively, in which the influence of in situ stresses, the unloading rate and path on the dynamic effects of excavation is examined. The similar numerical simulation is also conducted by the use of discrete element code PFC<sup>2D</sup> (Li et al. 2014a).

In reality, underground rock also experiences dynamic disturbance caused by mechanical shock and drilling and blasting operation. Using the self-invented SHPB device, Li et al. (2008) and Zhou et al. (2014) investigated the dynamic compressive and tensile behavior of rocks under different coupled static and dynamic loads. Yin et al. (2012a) analyzed the failure mechanism and failure surface morphology of highly stressed rocks subjected to unloading and dynamic disturbance, and they observed tensile failure or combined shear failure under low impact energy and tensile failure under high impact energy. The compression strength of sandstone subjected to dynamic disturbance after excavation was studied with the coupled dynamic and static loading split Hopkinson pressure bar system (Ye et al. 2013). The damage and failure process of rock under combined static and dynamic loading was also simulated by using the RFPA-Dynamics (Zhu et al. 2012).

The analytical solution and physical experiments are very important for the rock failure analysis under dynamic loading, especially for the excavation damage zone, but these boundary and initial conditions for the numerical

simulation on rock failure are too complex for the analytical and experimental approach to tackle. Therefore, it is difficult to give the mathematical model of rock failure in differential form and conduct the physical experiments under complex loading and unloading path. Compared with the experimental observation, failure process of rock can be easily examined with the numerical simulation; thus, the advantage of numerical simulation is highlighted. In this work, the failure process of rock sequentially subjected to the quasi-static triaxial loading before excavation, unloading of confining pressure and dynamic disturbance after excavation is simulated by the simulator RFPA-Dynamics, which makes it possible to reveal the damage and fracture mechanism of rock during this complex loading path.

### Model setup for rock under confined compression and unloading of confining pressure

Briefly, the simulator used in this work is a two-dimensional (2D) code that can simulate the fracture and failure process of rock under static, dynamic and combined static and dynamic loading conditions (Zhu et al. 2012). In RFPA-Dynamics, the rock specimen is assumed to be composed of many elements with the same size, and the mechanical properties of these elements are assumed to conform to a given Weibull distribution (Weibull 1951). The finite element method is employed to obtain the stress fields in the mesoscopic elements. Elastic damage mechanics is used to describe the constitutive law of the mesoscale elements when the maximum tensile strain criterion and the Mohr–Coulomb criterion that incorporate the effect of stress rate are utilized as damage thresholds (Zhu and Tang 2004). Flowchart for the coupled static and dynamic analysis of RFPA-Dynamics code has been given in the paper (Zhu et al. 2010).

More descriptions of the theoretical basis, capabilities and validations of RFPA and RFPA-Dynamics have been given in previous publications (Zhu and Tang 2004, 2006; Zhu et al. 2010). Therefore, detailed descriptions of RFPA-Dynamics, as well as its validation, are not presented here. Rather, the applicability of RFPA-Dynamics to simulate the failure process of rock under unloading of confining pressure and dynamic disturbance will be considered.

In this section, the numerical model is established according to previous experiments with sandstone conducted by Yin et al. (2012b) and Huang et al. (2011). The mass density of the specimen is  $2500 \text{ kg/m}^3$ . The uniaxial compressive strength (UCS) and tensile strength of the rock are 90.0 and 9.0 MPa, respectively. The Young's modulus, Poisson ratio and internal frictional angle of the specimen are 21.6 GPa,  $0.25^\circ$  and  $35^\circ$ , respectively.

The Young's modulus and uniaxial compressive strength can be simulated with a Weibull distribution with the parameters listed in Table 1 when the rock specimen is assumed heterogeneous. The corresponding means of the Young's modulus and strength are obtained from a trial-and-error simulation process in order to fit the physical-mechanical parameters of this rock. In this numerical simulation, no heterogeneity is incorporated in the mass density, Poisson's ratio and internal frictional angle, and the ratio of uniaxial compressive/tensile strength is assigned a constant of 10.

In order to reduce the computing efforts, the analyses presented here are performed under plane stress condition. As shown in Fig. 1, the rock specimen has a dimension of  $135 \text{ mm} \times 135 \text{ mm}$  and is composed of  $135 \times 135$  quadrilateral iso-parametric elements. The upper and bottom loading plates are stiff and with a width of 27 mm. The left and right loading plates are soft and with a width of 18 mm. The soft load-bearing plate with a width of 18 mm is sandwiched between the rock specimen and the right loading plate, where the unloading of the rock specimen in horizontal direction becomes possible by removing this plate instantly after the high confined pressure is applied.

### Validation of numerical simulator RFPA-dynamics

Previous study by Huang et al. (2011) indicated that the failure of rock under confined compression shows intensive dilatation along the unloading direction once the confining pressure is unloaded. In this section, the failure characteristics of rock specimens sequentially subjected to highly confined compression, unloading of confining stress and disturbance of dynamic loading are studied and are compared previous experimental results, in order to validate RFPA-Dynamics in simulating this kind of complex loading paths.

### The failure process of rock under quasi-static loading

The numerical simulation on the rock failure under uniaxial quasi-static loading is also achieved with the model setup as shown in Fig. 1, in which, however, the left and right sides of the specimen are free from the confinement of soft load-bearing plates. An external displacement is applied at a constant rate of  $0.005 \text{ mm/step}$  in the vertical direction until the rock specimen fails.

The stress–strain curve of rock specimen under uniaxial compression is shown in Fig. 2. The stress–strain curve is basically linear until peak loading is attained. Then, the specimen loses its loading capacity substantially because

**Table 1** Weibull distribution parameters of heterogeneous rock specimen

Homogeneity index $m$	Means of Young's modulus (GPa)	Means of uniaxial compressive strength (MPa)	Poisson's ratio	Internal frictional angle ( $^{\circ}$ )
5	24.69	203.57	0.25	35

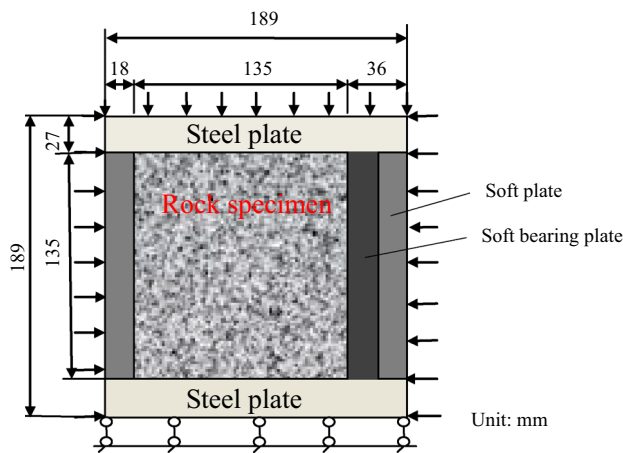


**Fig. 1** Model setup of the numerical simulation

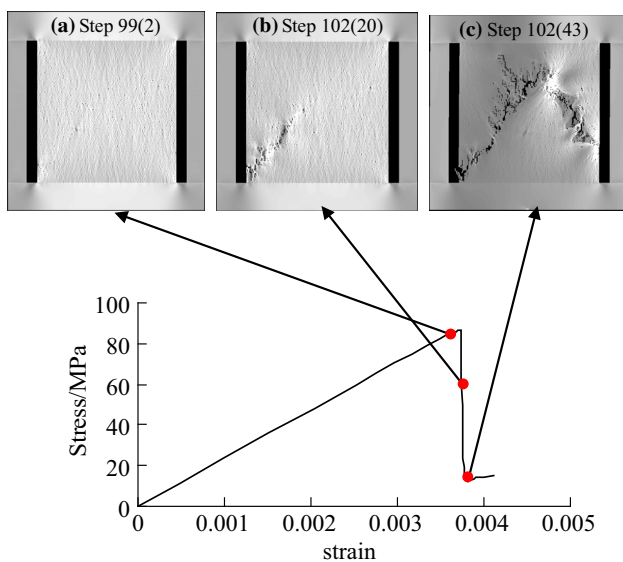


**Fig. 2** The stress–strain curve and failure pattern of specimen under uniaxial compression loading

the specimen is relatively brittle. The uniaxial compressive strength of the specimen is 86.98 MPa, and it approximates the experimental result given by Yin et al. (2012b).

As shown in Fig. 2, the isolated damages initiate near the surface in the lower left corner of the specimen and then propagate diagonally upwards to the center of the specimen. A shear damage zone is also developed at the lower right corner of the specimen and propagates diagonally upwards to interconnect with the former damage

zone. At last, an X-shaped damage zone that looks like a shear failure zone is formed, leading to the failure of this rock specimen.

**The failure process of rock under dynamic loading after confining pressure unloading**

In this section, the rock specimen is firstly subjected to confined compression. The boundary stresses in the vertical and horizontal directions, denoted with  $p_s$  and  $\kappa p_s$  ( $\kappa$  is called lateral pressure coefficient), respectively, are applied incrementally until pre-specified quasi-static stresses are attained. The vertical stress ( $p_s$ ) is 54 MPa and approximately equals to sixty percent of the uniaxial compressive strength. The lateral pressure coefficient ( $\kappa$ ) is 0.74. The bottom and right sides of the model domain are prevented from displacement in the vertical and horizontal directions, respectively. Then, the unloading of confining pressure is achieved through removing the soft load-bearing plate. At last, the dynamic incident stress pulse  $p_d(t)$  as shown in Fig. 3, obtained from the previous published (Yin et al. 2012b; Ye et al. 2013), is applied at the top surface of a model domain after confining pressure unloading. As for the dynamic loading condition, the bottom surface of the domain is fixed in vertical direction.

The failure patterns, together with the damage zone, elastic modulus and maximum shear stress distribution during the failure process of rock, are shown in Fig. 4. At  $t = 0 \mu s$ , the confining pressure is unloaded, and the dynamic stress wave is applied. The rock specimen does not fail after confining pressure unloading, but there is tensile damage zones appearing near the free surface in the

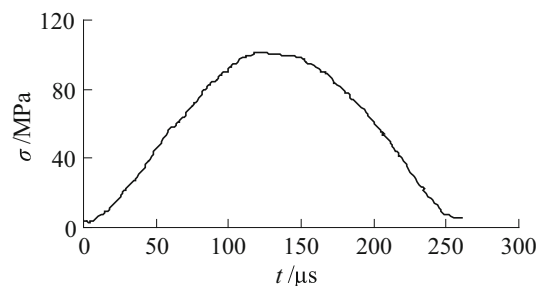


**Fig. 3** The incident stress wave applied in numerical simulation and obtained from the previous published (Yin et al. 2012b; Ye et al. 2013)

**Fig. 4** Distribution of damage, elastic modulus and maximum shear stress during the failure of rock specimen under dynamic loading after confining pressure unloading

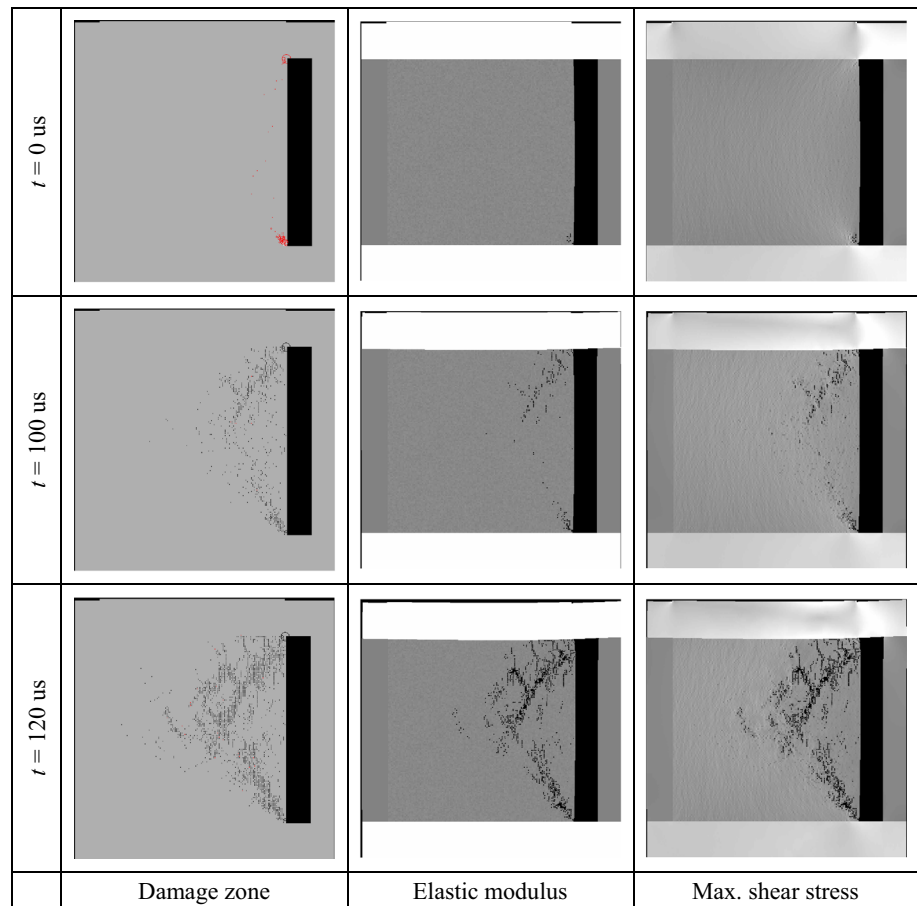


**Fig. 5** Typical failure pattern of sandstone under dynamic loading after confining pressure unloading (Yin et al. 2012b)

upper and lower right corner. Then, this damage zone at the upper right corner of the specimen develops further inwards into rock after the dynamic disturbance is applied at top of the domain in vertical direction. However, the damage zone at the lower right corner does not develop until the dynamic stress wave travels toward this location around  $t = 100 \mu\text{s}$ . When  $t = 125 \mu\text{s}$ , the arc-shaped damage zone is observed near the free face. If the rock

specimen is subjected to the unloading of confining pressure symmetrically at left and right sides, two arc-shaped damage zones will develop symmetrically at both the left and right sides of the specimen. In that case, finally, the failure mode of the rock specimen would be similar to the experimental observation given by Yin et al. (2012b), as shown in Fig. 5.

In general, the acceptable agreement between the experimental and numerical observations confirms the capability of RFPA-Dynamics in reproducing the failure process of rock sequentially subjected to the quasi-static triaxial loading, unloading of confining pressure and disturbance of dynamic loading.

**Further simulation on the rock specimen under complex loading paths**

In this section, numerical simulation of rock failure under different loading paths in terms of dynamic loading after confined compression and confining pressure unloading is discussed. The axial pressures ( $p_s$ ) of 16.0, 32.0 and 48.0 MPa are, respectively, applied step by step at the top

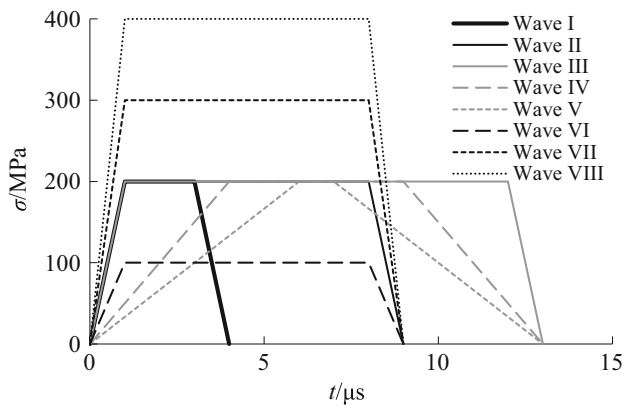


**Fig. 6** The incident stress waves applied at the top surface of the model domain with different amplitudes and durations

of the rock specimen in vertical direction, while the confining pressure coefficient  $\kappa = 0.3, 1.0$  and  $1.5$  is specified. After a specific static stress level is attained, the confining pressure unloads, and then, a dynamic incident stress wave is applied at the top surface. The development of excavation damaged zone is mainly influenced by the dynamic disturbance under the low in situ stress conditions. The rectangle wave and triangular wave can be simplified as impacting loading during the impacting tests and are regarded as the special trapezoidal wave through adjusting the rising time, falling time and constant time. In order to clarify the effect of waveforms of incident waves on the rock failure, the incident stress waveform, as shown in Fig. 6, is applied. The amplitudes of the incident stress pulses  $p_{dm} = 100, 200, 300$  and  $400$  MPa are specified,

**Fig. 7** The failure processes of rocks subjected to complex loading paths with various axial loading

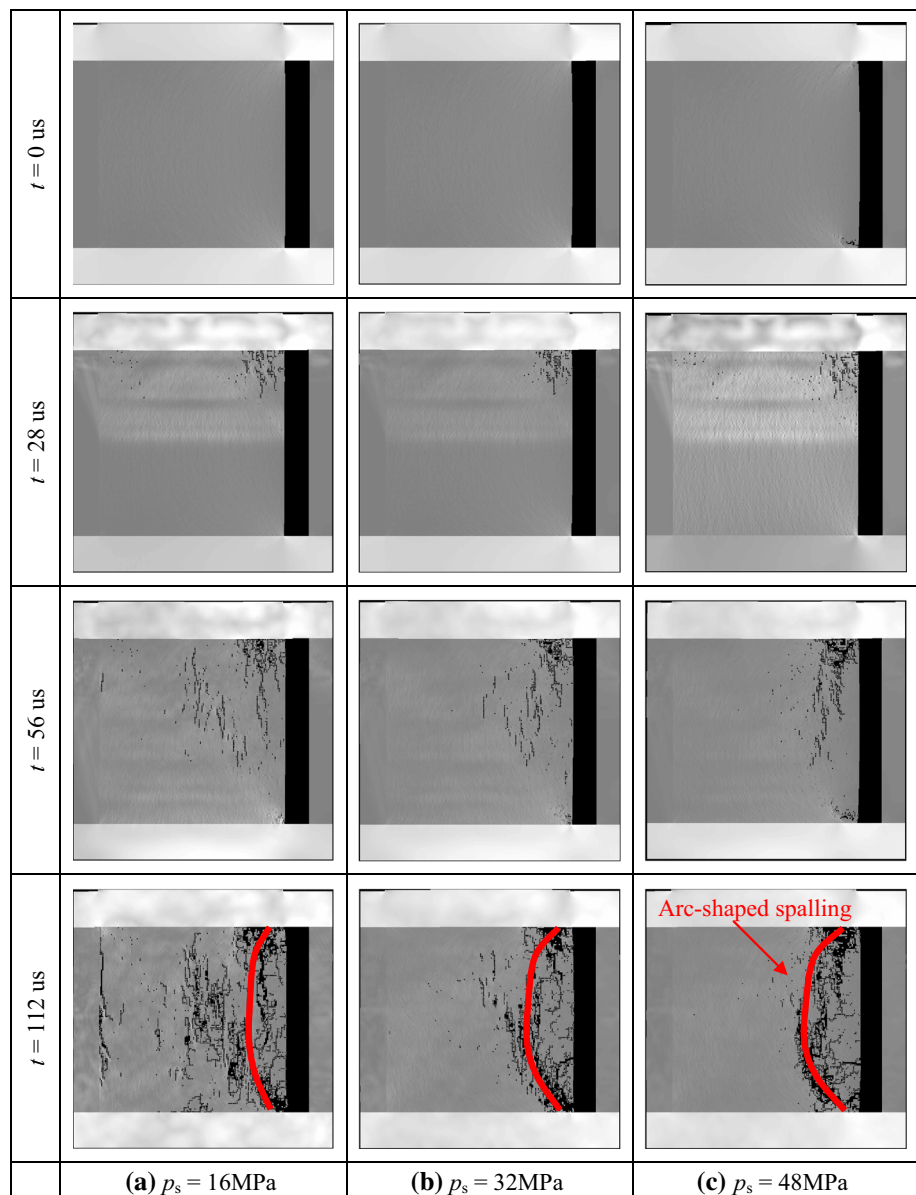
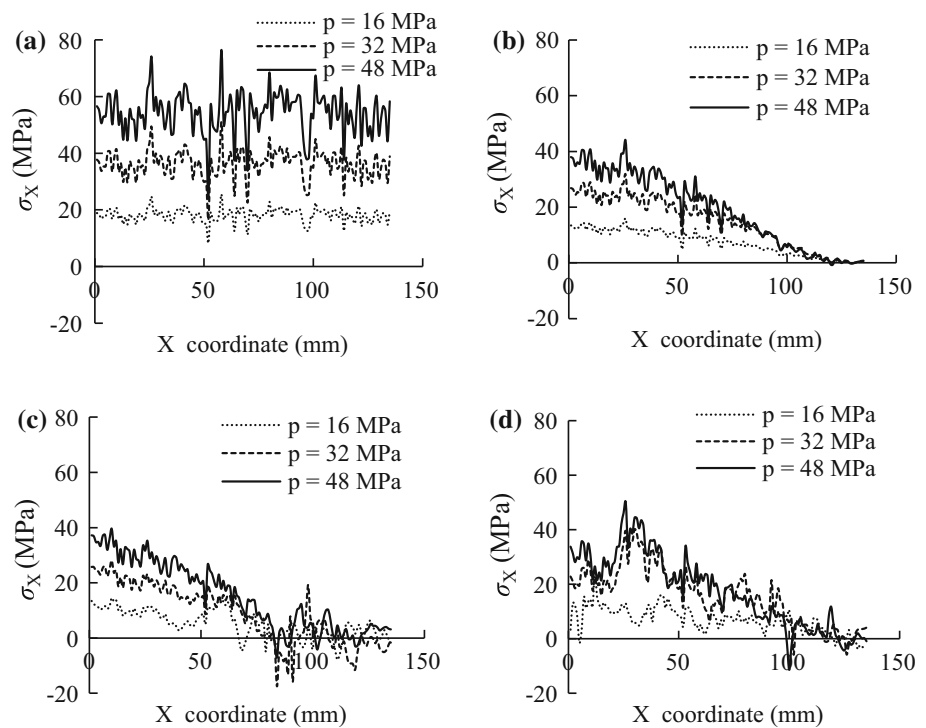


**Fig. 8** Stresses in X-direction  $\sigma_x$  along the horizontal line crossing the center of the specimen subjected to complex loading paths with various axial loadings. **a** The final step under static loading, **b**  $t = 0 \mu\text{s}$ , **c**  $t = 56 \mu\text{s}$ , **d**  $t = 112 \mu\text{s}$



while the time durations of the stress pulses  $t_{dm} = 4, 9$  and  $13 \mu\text{s}$  are selected.

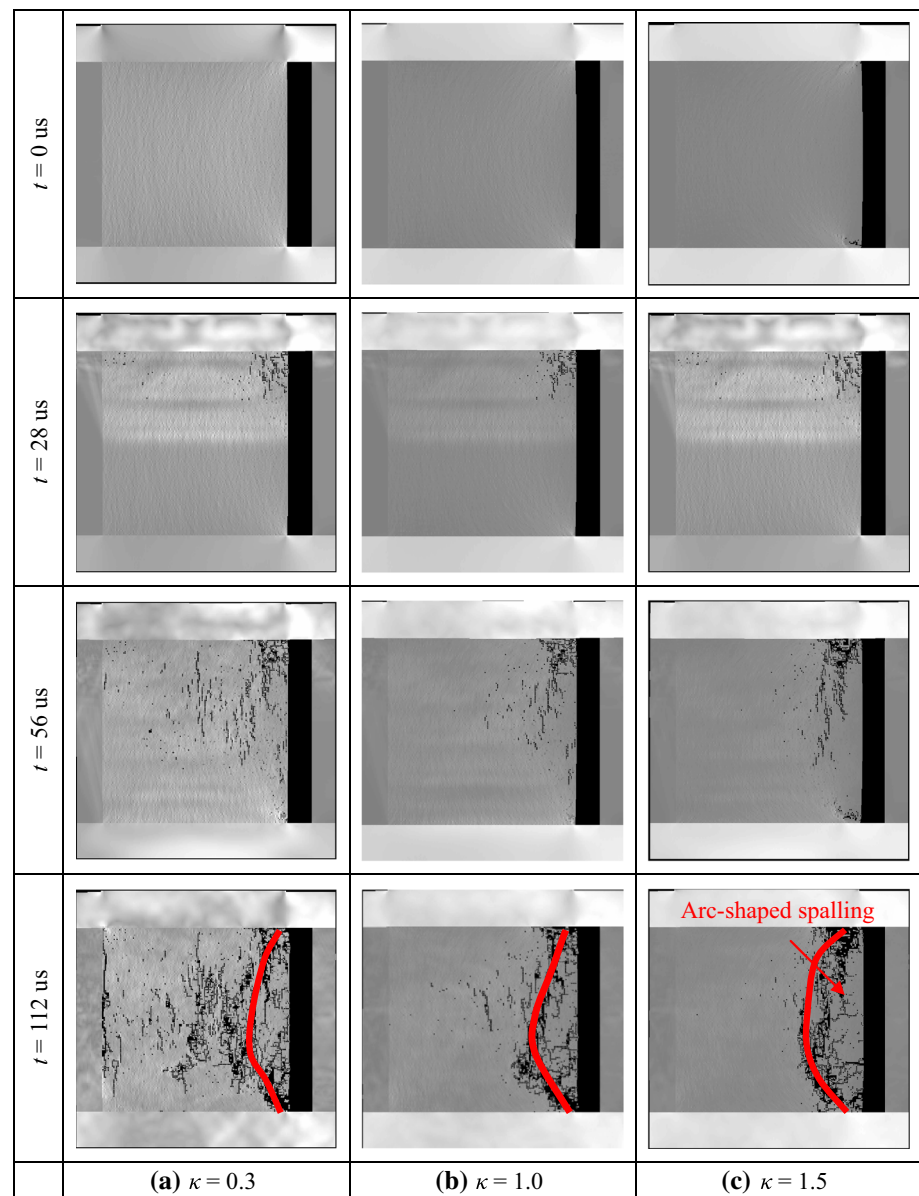
**Effect of the axial pressure**

Figure 7 shows the failure process of the rock specimen subjected to complex loading paths with various axial pressures while  $\kappa = 1.5$ . The axial pressures  $p_s = 16.0, 32.0$  and  $48.0 \text{ MPa}$  are applied, based on which the corresponding overburden depth is 640, 1280 and 1920 m, respectively. The incident stress wave II in Fig. 6 is applied, where  $p_{dm} = 200.0 \text{ MPa}$  and  $t_{dm} = 9 \mu\text{s}$ , and the failure process of rock specimen under different in situ stress conditions and a specific dynamic disturbance is investigated as shown in Fig. 7.

From Fig. 7, at  $t = 0 \mu\text{s}$ , the damage initiates near the free surface in the upper and lower right corner of the specimen under the higher axial pressure of  $p_s = 48.0 \text{ MPa}$ ; however, it does not when  $p_s = 16.0$  and  $32.0 \text{ MPa}$ . This indicates that the initiation of this initial damage after confining pressure unloading is closely related to the axial pressure. The effect of the confining pressure unloading becomes more pronounced under the initial high axial pressure, since more energy is stored during the quasi-static loading stage. At  $t = 28 \mu\text{s}$ , the dynamic stress wave propagates downwards until the half height of the specimen. The damage zone is developed near the upper end of the specimen, and it propagates downwards, forming some vertical cracks, which is due to the tensile damage induced

by high compressive stress in axial direction. This kind of axial crack is restrained under the higher axial stress, because the more pronounced confinement occurs under the higher axial pressure, as shown in Fig. 8. Figure 8 presents the distribution of stress ( $\sigma_x$ ) in X-direction along the horizontal line crossing the center of the specimen. Stress  $\sigma_x$  becomes higher with axial pressure until the specific static stress level is attained, as shown in Fig. 8a. When the dynamic loading is applied, the stress  $\sigma_x$  decreases along the X-direction; however, its confinement on the left part of the specimen becomes more pronounced under the higher axial pressure. In general, as shown in Fig. 7a, the tensile crack initiates parallel to the axial loading direction, especially at the left half of the specimen, followed by the arc-shaped spalling cracks initiated at the right unloading surface after confining pressure unloading. In this regard, the volume of arc-shaped failure zone increases and the number of axial cracks decreases with the rising axial pressure, denoting that the high axial pressure tends to promote the arc-shaped failure zone but restrain axial cracks. It is worth mentioning that under the low axial pressure, the axial cracks are connected with the arc-shaped spalling cracks, reflecting the interaction between these two kinds of cracking mechanisms. This denotes that the failure mode of the rock specimen under this complex loading path depends on the axial pressure under dynamic disturbance after confining pressure unloading.

**Fig. 9** The failure processes of rocks subjected to complex loading paths with various confining pressures (lateral pressure coefficient)



Before the dynamic stress wave is applied, the rock specimen is intact even though the confining pressure is unloaded, as shown in Fig. 7 ( $t = 0 \text{ us}$ ), thus confirming the contribution of dynamic stress wave in triggering the arc-shaped spalling. In this respect, because quasi-static axial pressure is not provide sufficient energy for the rock failure during confining pressure unloading, the further inpouring of energy due to dynamic disturbance is an important factor to trigger the rock failure.

#### Effect of the lateral pressure coefficient

In this section, the axial pressure is a constant of  $p_s = 48 \text{ MPa}$ , and the lateral pressure coefficients of  $\kappa = 0.3, 1.0$  and  $1.5$  are applied. As for dynamic

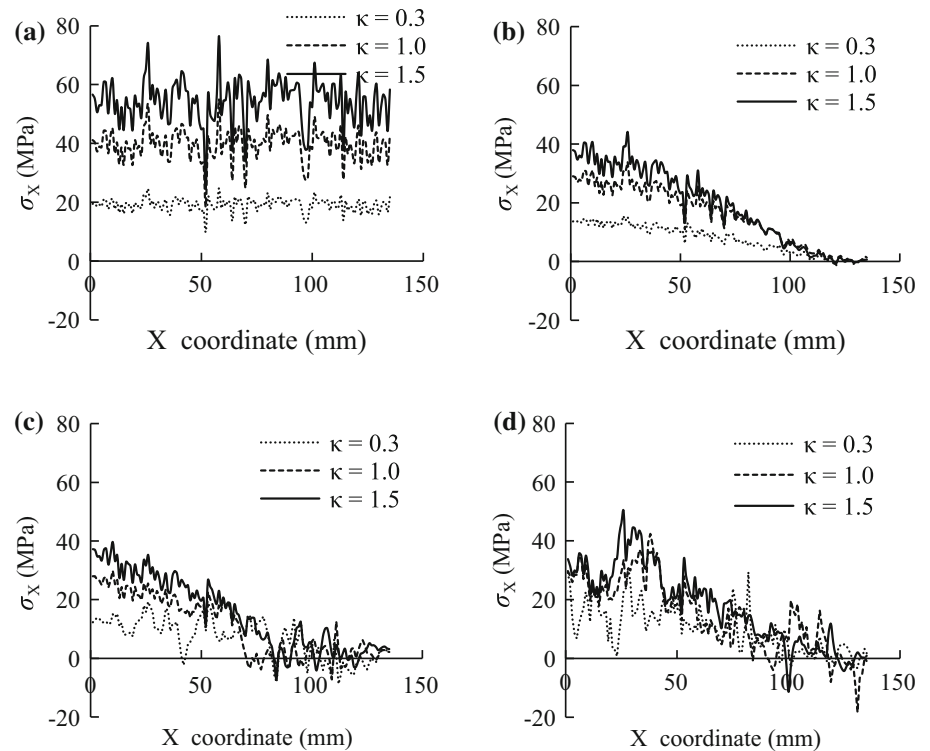
disturbance, the incident stress wave II as shown in Fig. 6 is also applied.

As shown in Fig. 9, only at the lateral pressure coefficient of  $\kappa = 1.5$ , the unloading of confining pressure leads to the damage zone initiation near the free surface in the upper and lower right corner of the specimen. This denotes that, similar to the contribution of high axial pressure, the high confining pressure is also a main factor to induce the failure after excavation, because both the axial pressure and confining pressure may contribute to the accumulation of elastic strain energy in the rock prior to unloading.

Under different lateral pressure coefficients, the arc-shaped spalling cracks near the right free surface are developed, and the area of them increases with the lateral pressure coefficient. However, the axial cracks are



**Fig. 10** Stresses in X-direction  $\sigma_x$  along the horizontal line crossing the center of the specimen subjected to complex loading paths with various confining pressures. **a** The final step under static loading, **b**  $t = 0 \mu\text{s}$ , **c**  $t = 56 \mu\text{s}$ , **d**  $t = 112 \mu\text{s}$



developed more evident under the low lateral pressure coefficients, i.e.,  $\kappa = 0.3$ , which may also interconnect with the arc-shaped spalling crack at  $t = 112 \mu\text{s}$ . This kind of axial crack is restrained under the higher lateral pressure coefficient, as shown in Fig. 10, because the stress  $\sigma_x$  at the left of the specimen becomes higher under the higher lateral pressure coefficient.

In general, in situ stress dominates the quasi-static stress distribution around excavation surface before unloading, while the dynamic disturbance applied in this manner may trigger the arc-shaped spalling zone at the right of the rock specimen and enhance the axial crack propagation at the left half of the specimen. Under the small lateral pressure coefficient, the axial cracks propagate mainly due to the triggering action of the dynamic disturbance. With the increase in lateral coefficient, the higher compressive stresses at the left of the specimen that are induced by in situ stress may restrain the tensile stress triggered by dynamic disturbance, thus preventing the initiation of axial cracks.

**Effect of the duration of the incident stress wave**

The maximum shear stresses during failure process of the rock specimen under different durations of dynamic disturbances are shown in Fig. 11. In this section, the axial pressure  $p_s = 48 \text{ MPa}$  and  $\kappa = 1.5$ . The incident stress wave as

shown in Fig. 6 is applied at the top surface of the model domain, while  $p_{dm} = 200 \text{ MPa}$  and  $t_{dm} = 4, 9$  and  $13 \mu\text{s}$ .

When  $t = 0 \mu\text{s}$ , the stress distributions of rock specimens are same, since they are subjected to the same in situ stress and confining pressure unloading. As shown in Fig. 11, at  $t = 28 \mu\text{s}$ , the failure mode of rock specimens is similar although the duration of the incident stress waves is different. Under the same amplitude of the incident stress wave ( $p_{dm}$ ), the more energy is input into the rock specimen if the duration of the incident stress wave ( $t_{dm}$ ) is prolonged. So the area of arc-shaped spalling zone increases with the prolonged duration of the incident stress wave. But the arc-shaped spalling zones all initiate at the upper right corner near the free surface and terminate at the lower right corner. It indicates that the shape and area of the arc-shaped spalling zone are influenced by the duration of the incident wave. Under these loading conditions, as shown in Fig. 11, the axial crack is restrained in despite of the duration of stress wave, because the stresses  $\sigma_x$  at the left part of specimen are so high that the rock is horizontally confined, as shown in Fig. 12. This also indicates that the initiation of axial crack is mainly dominated by in situ stress conditions before excavation.

The incident waves III, IV and V, as shown in Fig. 6, are applied in order to study the dynamic response of rock specimen under different durations of dynamic disturbance.

**Fig. 11** The failure processes of rocks subjected to complex loading paths with various durations of stress wave

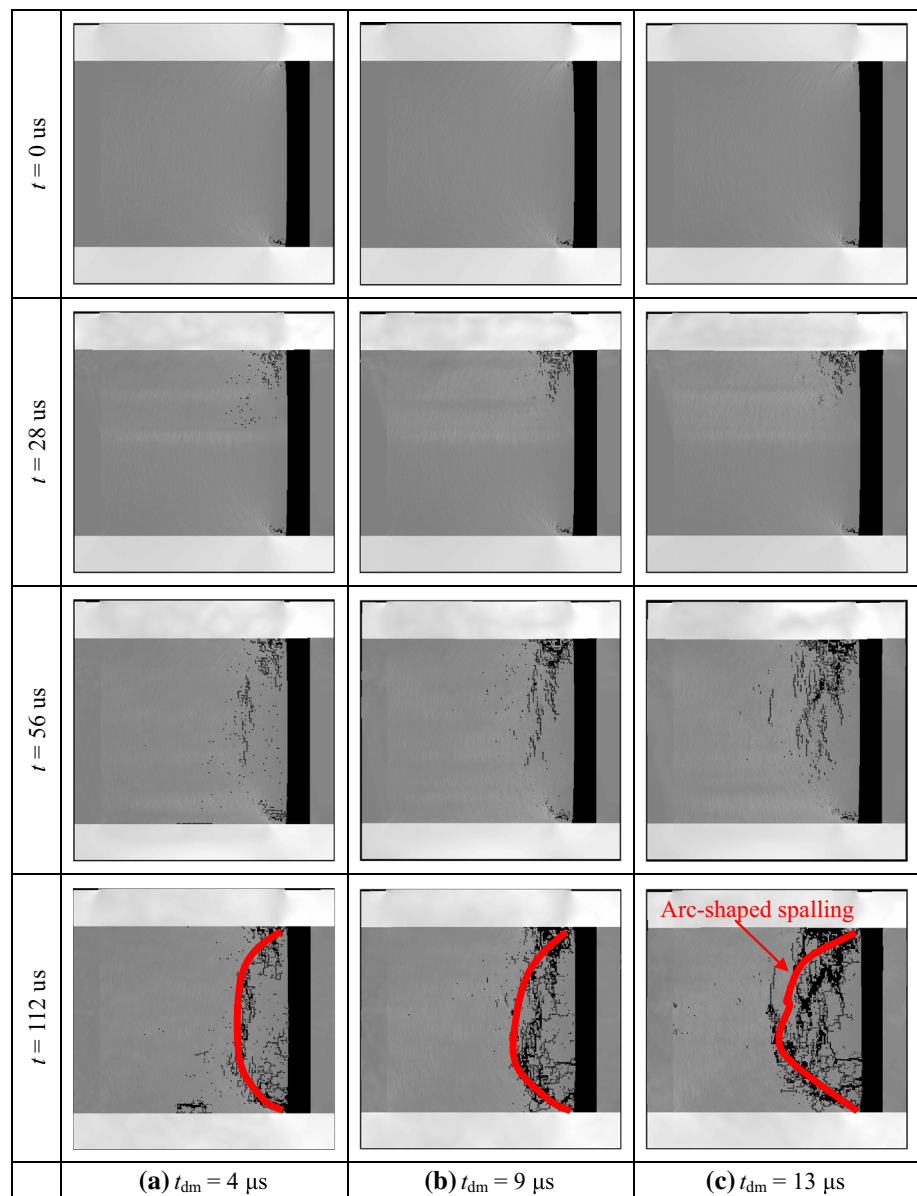
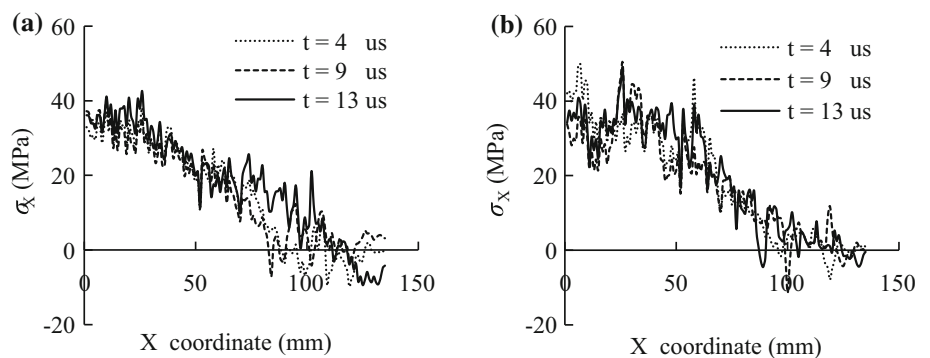


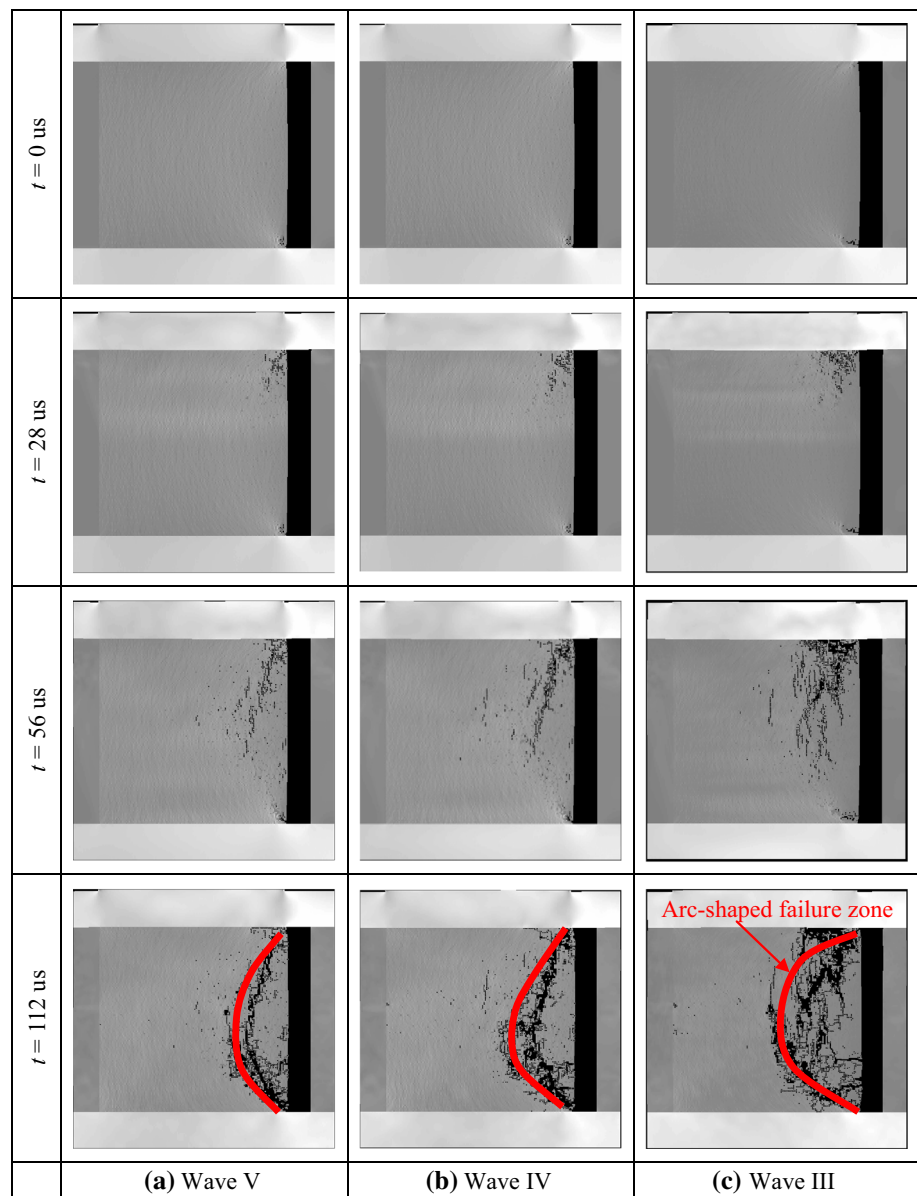
**Fig. 12** Stresses in X-direction  $\sigma_x$  along the horizontal line crossing the center of the specimen subjected to complex loading paths with various durations of stress wave. **a**  $t = 56 \mu s$ , **b**  $t = 112 \mu s$



Here, the axial pressure  $p_s = 48 \text{ MPa}$  and  $\kappa = 1.5$ . The less energy is input into the rock specimen if the rising time is prolonged under the same amplitude and duration of the

incident wave. It indicates that shapes of the arc-shaped spalling zones are similar and areas of those increase with decreasing rising time, as shown in Fig. 13.

**Fig. 13** The failure processes of rocks subjected to complex loading paths with various rising times of stress wave



**Effect of the amplitude of the incident stress wave**

In this section, the axial pressure is a constant of  $p_s = 48 \text{ MPa}$  while  $\kappa = 1.5$ . The incident stress wave VI, II, VII and VIII as shown in Fig. 6 is applied where its duration is a constant of  $t_{dm} = 9 \text{ }\mu\text{s}$  while  $p_{dm} = 100, 200, 300 \text{ and } 400 \text{ MPa}$ , respectively.

Under the same duration of the incident stress wave, the energy input into the rock specimen increases with the amplitude of the incident stress wave ( $p_{dm}$ ) at the same time range. As shown in Fig. 14, the arc-shaped spalling zone becomes larger under longer duration of the incident stress wave, because more energy is input.

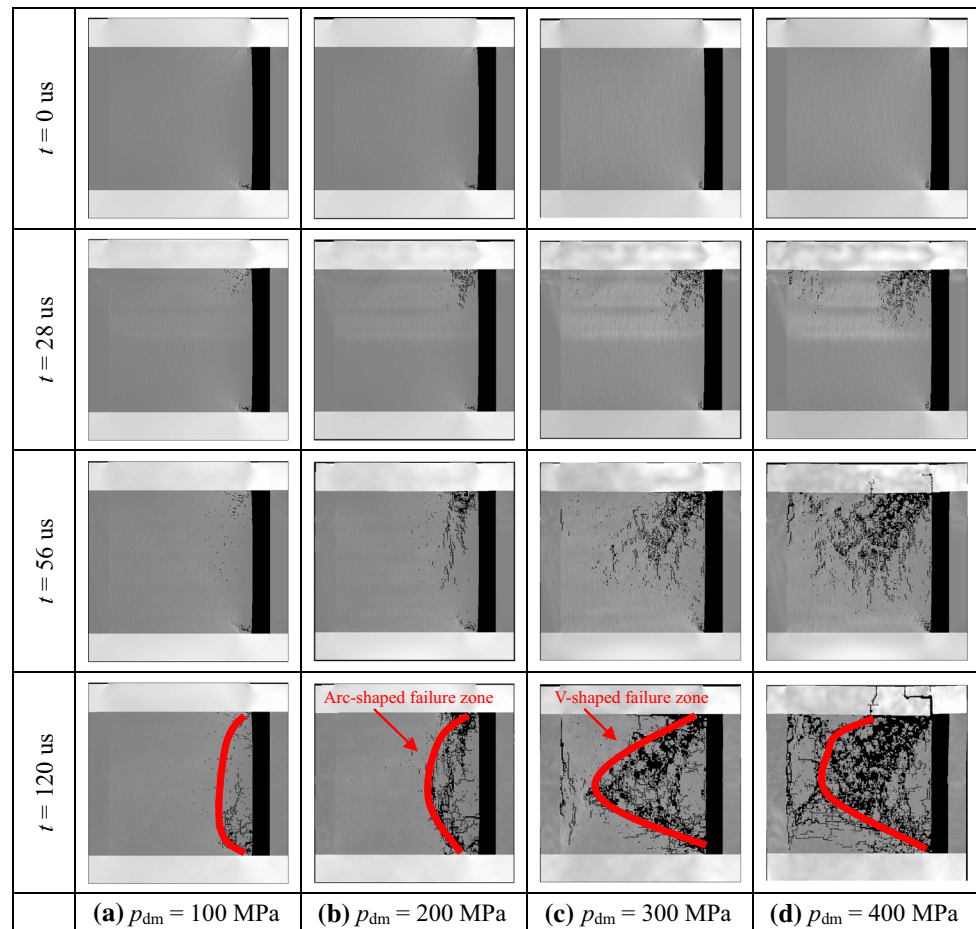
As a whole, developments of shape and area of the arc-shaped damage zones are similar under different durations

and amplitudes of dynamic disturbance as shown in Figs. 11, 13 and 14. It indicates that the arc-shaped damage zone is dominated by the energy input into the rock specimen under the dynamic disturbance after the same confining stress unloading, and influences of the duration and amplitude of incident stress wave on the failure pattern are similar because they all contribute to the energy input.

**Conclusions**

The failure of rock sequentially subjected to the complex quasi-static and dynamic loading paths is numerically simulated by using the numerical simulator RFPD-Dynamics. The influences of the quasi-static in situ stress

**Fig. 14** The failure processes of rocks subjected to complex loading paths with various amplitudes of stress wave



conditions before excavation and the waveform of the dynamic disturbance on the rock failure are examined. This kind of work is of great significance to clarify the rock failure mechanism during this complex loading path of rock such as the excavation of underground opening. Based on the numerical simulations, the following conclusions can be drawn from the numerical simulations:

1. The numerical model established by using RFPD-Dynamics is used to simulate the failure of rock sequentially subjected to the quasi-static triaxial loading, confining pressure unloading and dynamic loading. The acceptable agreement between experimental and numerical results shows that RFPD-Dynamics is capable of reproducing the failure process of rock, thus confirming RFPD-Dynamics as an eligible candidate to simulate the failure process of rock triggered by dynamic disturbance after confining pressure unloading.
2. When the confining pressure is unloaded, the arc-shaped spalling damage zone is prone to develop with the increase in the axial pressure and lateral pressure

coefficient, but the axial crack tends to be restrained by the horizontal stress in the rock specimen.

3. After rock specimen subjected to the same in situ stress and confining stress unloading, the effect of the duration and amplitude of dynamic disturbance on the energy input is similar and the area of the arc-shaped spalling zone of rock specimen is dominated by the energy input into the rock specimen. Altogether, during the excavation of underground opening, the shape and area of the excavation damaged zone may be influenced by in situ stress condition and waveform of dynamic disturbance.

Compared to the experiment conducted by Yin et al. (2012b), the more complex loading and unloading path can be carried out, and the failure process of rock can be observed and clarified by using the numerical simulation. But it is still difficult to be used to solve the engineering problems, such as the failure of rock mass induced by the blasting (Lapčević et al. 2014) and earthquake (Kostić et al. 2013). The application of numerical simulation method for the engineering problem would be studied further.

Although the numerical simulation is two-dimensional and the engineering problem is three-dimensional, the rock failure mechanism during this the excavation process is fairly similar. Accordingly, the 2D numerical and experimental results, it is really helpful for understanding different mechanisms associated with the excavation-induced damage zone. Moreover, since underground openings are always 3D geometries and undergo 3D geo-stress condition, in the long run, the 3D simulations should be done to characterize the more realistic failure patterns.

**Acknowledgements** This work is funded by the National Key Research and Development Program of China (Grant No. 2016YFC0801607), National Science Foundation of China (Grant Nos. 51525402, 51374049, 51474051 and 51534003), the Key Project of Chinese Ministry of Education (No. 113019A) and the Fundamental Research Funds for the Central Universities of China (Grant Nos. N160104008, N160103005). These supports are gratefully acknowledged.

## References

- Backblom G, Martin CD (1999) Recent experiments in hard rocks to study the excavation response: implications for the performance of a nuclear waste geological repository. *Tunn Undergr Space Technol* 14:377–394
- Bossart P, Meier PM, Moeri A, Trick T, Mayor JC (2002) Geological and hydraulic characterisation of the excavation disturbed zone in the Opalinus Clay of the Mont Terri Rock Laboratory. *Eng Geol* 66:19–38
- Cai M, Kaiser PK (2005) Assessment of excavation damaged zone using a micromechanics model. *Tunn Undergr Space Technol* 20:301–310
- Corkum AG, Martin CD (2007a) The mechanical behaviour of weak mudstone (Opalinus Clay) at low stresses. *Int J Rock Mech Min Sci* 44:196–209
- Corkum AG, Martin CD (2007b) Modelling a mine-by test at the Mont Terri rock laboratory, Switzerland. *Int J Rock Mech Min Sci* 44(6):846–859
- Diederichs MS, Kaiser PK, Eberhardt E (2004) Damage initiation and propagation in hard rock during tunnelling and the influence of near-face stress rotation. *Int J Rock Mech Min Sci* 41(5):785–812
- Fakhimi A, Carvalho F, Ishida T, Labuz JF (2002) Simulation of failure around a circular opening in rock. *Int J Rock Mech Min Sci* 39:507–515
- Falls SD, Young RP (1998) Acoustic emission and ultrasonic-velocity methods used to characterize the excavation disturbance associated with deep tunnels in hard rock. *Tectonophysics* 289:1–15
- Forquin P, Gary G, Gatuingt F (2008) A testing technique for concrete under confinement at high rates of strain. *Int J Impact Eng* 35:425–446
- Frew DJ, Akers SA, Chen W, Green ML (2010) Development of a dynamic triaxial Kolsky bar. *Meas Sci Technol* 21(10):105704. doi:10.1088/0957-0233/21/10/105704
- Guan Z, Jiang Y, Tanabasi Y (2007) Ground reaction analyses in conventional tunnelling excavation. *Tunn Undergr Space Technol* 22:230–237
- He MC, Zhao F (2013) Laboratory study of unloading rate effects on rockburst. *Disaster Adv* 6:11–18
- He MC, Miao JL, Feng JL (2010) Rock burst process of limestone and its acoustic emission characteristics under true-triaxial unloading conditions. *Int J Rock Mech Min Sci* 47(2):286–298
- Hing LK, Othman SZ, Hashim R, Ismail Z (2014) Determination of soil stiffness parameters at a deep excavation construction site in Kenny Hill Formation. *Measurement* 47:645–650
- Hua AZ, You MQ (2001) Rock failure due to energy release during unloading and application to underground rock burst control. *Tunn Undergr Space Technol* 16(3):241–246
- Huang D, Li YR (2014) Conversion of strain energy in triaxial unloading tests on marble. *Int J Rock Mech Min Sci* 66:160–168
- Huang RQ, Wang XN, Chan LS (2001) Triaxial unloading test of rocks and its implication for rock burst. *Bull Eng Geol Environ* 60:37–41
- Huang ZP, Tang CA, Ma TH, Tang LX (2011) Numerical test investigation on unloading rockburst processes. *Chin J Rock Mech Eng* 30(1):3120–3128
- Kim Y, Amadei B, Pan E (1999) Modeling the effect of water, excavation sequence and rock reinforcement with discontinuous deformation analysis. *Int J Rock Mech Min Sci* 36:949–970
- Kostić S, Vasović N, Perc M, Toljić M, Nikolić D (2013) Stochastic nature of earthquake ground motion. *Physica A* 392:4134–4145
- Labieuse V, Vietor T (2014) Laboratory and in situ simulation tests of the excavation damaged zone around galleries in opalinus clay. *Rock Mech Rock Eng* 47:57–70
- Lapčević R, Kostić S, Pantović R, Vasović N (2014) Prediction of blast-induced ground motions in a copper mine. *Int J Rock Mech Min Sci* 69:19–25
- Li XB, Zhou ZL, Lok TS, Hong L, Yin TB (2008) Innovative testing technique of rock subjected to coupled static and dynamic loads. *Int J Rock Mech Min Sci* 45(5):739–748
- Li XB, Cao WZ, Zhou ZL, Zou Y (2014a) Influence of stress path on excavation unloading response. *Tunn Undergr Space Technol* 42:237–246
- Li XJ, Yang WM, Wang LG, Butler IB (2014b) Displacement forecasting method in brittle crack surrounding rock under excavation unloading incorporating opening deformation. *Rock Mech Rock Eng* 47:2211–2223
- Malmgren L, Saiang D, Toyra J, Bodare A (2007) The excavation disturbed zone (EDZ) at Kiirunavaara mine, Sweden—by seismic measurements. *J Appl Geophys* 61(1):1–15
- Martino JB, Chandler NA (2004) Excavation-induced damage studies at the underground research laboratory. *Int J Rock Mech Min Sci* 41:1413–1426
- Read RS (2004) 20 years of excavation response studies at AECL's underground research laboratory. *Int J Rock Mech Min Sci* 41:1251–1275
- Sazzad MM (2014) Micro-scale behavior of granular materials during cyclic loading. *Particuology* 16:132–141
- Sellers EJ, Klerck P (2000) Modelling of the effect of discontinuities on the extent of the fracture zone surrounding deep tunnels. *Tunn Undergr Space Technol* 15:463–469
- Tao M, Li XB, Wu CQ (2012) Characteristics of the unloading process of rocks under high initial stress. *Comput Geotech* 45:83–92
- Tao M, Li X, Li D (2013) Rock failure induced by dynamic unloading under 3D stress state. *Theoretical and Applied Fracture Mechanics* 65:47–54
- Varas F, Alonso E, Alejano LR, Fdez-Manín G (2005) Study of bifurcation in the problem of unloading a circular excavation in a strain-softening material. *Tunn Undergr Space Technol* 20:311–322
- Vrakas A, Anagnostou G (2014) A finite strain closed-form solution for the elastoplastic ground response curve in tunneling. *Int J Numer Anal Methods Geomech* 38:1131–1148

- Weibull W (1951) A statistical distribution function of wide applicability. *J Appl Mech* 18:293–297
- Wu FQ, Liu T, Liu JY, Tang XL (2009) Excavation unloading destruction phenomena in rock dam foundations. *Bull Eng Geol Environ* 68(2):257–262
- Xie HQ, He C (2004) Study of the unloading characteristics of a rock mass using the triaxial test and damage mechanics. *Int J Rock Mech Min Sci* 41:13–18
- Yang HQ, Zeng YY, Lan YF, Zhou XP (2014) Analysis of the excavation damaged zone around a tunnel accounting for geostress and unloading. *Int J Rock Mech Min Sci* 69:59–66
- Ye ZY, Zhao FJ, Zhou ZL (2013) Mechanical characteristics of unloading rock under coupled dynamic and static loads. *Chin J Geotech Eng* 35(3):454–459
- Yin ZQ, Li XB, Jin JF, He XQ, Du K (2012a) Failure characteristics of high stress rock induced by impact disturbance under confining pressure unloading. *Trans Nonferrous Met Soc China* 22:175–184
- Yin ZQ, Li XB, Yin TB, Jin JF, Du K (2012b) Critical failure characteristics of high stress rock induced by impact disturbance under confining pressure unloading. *Chin J Rock Mech Eng* 31(7):1355–1362
- Zhao JD, Wang G (2010) Unloading and reverse yielding of a finite cavity in a bounded cohesive-frictional medium. *Comput Geotech* 37(1–2):239–245
- Zhou XP, Shou YD (2013) Excavation-induced zonal disintegration of the surrounding rock around a deep circular tunnel considering unloading effect. *Int J Rock Mech Min Sci* 64:246–257
- Zhou XP, Zhang YX, Ha QL (2008) Real-time computerized tomography (CT) experiments on limestone damage evolution during unloading. *Theor Appl Fract Mech* 50(1):49–56
- Zhou ZL, Li XB, Zou Y, Jiang YH, Li GN (2014) Dynamic Brazilian tests of granite under coupled static and dynamic loads. *Rock Mech Rock Eng* 47:495–505
- Zhu WC, Tang CA (2004) Micromechanical model for simulating the fracture process of rock. *Rock Mech Rock Eng* 37(1):25–56
- Zhu WC, Tang CA (2006) Numerical simulation of Brazilian disk rock failure under static and dynamic loading. *Int J Rock Mech Min Sci* 43(2):236–252
- Zhu WC, Li ZH, Zhu L, Tang CA (2010) Numerical simulation on rockburst of underground opening triggered by dynamic disturbance. *Tunn Undergr Space Technol* 25(5):587–599
- Zhu WC, Bai Y, Li XB, Niu LL (2012) Numerical simulation on rock failure under combined static and dynamic loading during SHPB tests. *Int J Impact Eng* 49:142–157
- Zhu WC, Wei J, Zhao J, Niu LL (2014a) 2D numerical simulation on excavation damaged zone induced by dynamic stress redistribution. *Tunn Undergr Space Technol* 43:315–326
- Zhu WS, Yang WM, Li XJ, Xiang L, Yu DJ (2014b) Study on splitting failure in rock masses by simulation test, site monitoring and energy model. *Tunn Undergr Space Technol* 41:152–164